

Thermal structure and basal sliding parametrisation at Pine Island Glacier - a 3D full-Stokes model study

N. Wilkens^{1,2}, J. Behrens³, T. Kleiner², D. Ripplin⁴, M. Rückamp², and A. Humbert^{2,5}

¹Institute for Geophysics, University of Hamburg, Germany

²Alfred Wegener Institute, Helmholtz Centre for Polar and Marine Research, Bremerhaven, Germany

³Numerical Methods in Geosciences, University of Hamburg, Germany

⁴Environment Department, University of York, Heslington, UK

⁵Department of Geosciences, University of Bremen, Germany

Correspondence to: Nina Wilkens (nina.wilkens@zmaw.de)

Abstract

Pine Island Glacier is one of the fastest changing glaciers in the Antarctic Ice Sheet and therefore in scientific focus. The glacier holds enough ice to raise global sea level significantly (~ 0.5 m), when fully melted. The question addressed by numerous modelling studies of the glacier focusses on whether the observed changes are a start for an uncontrolled and accelerating retreat. The movement of the glacier is, in the fast flowing areas, dominated by basal motion. In modelling studies the parametrisation of the basal motion is therefore crucial. Inversion methods are commonly applied to reproduce the complex surface flow structure at Pine Island Glacier, which use information of the observed surface velocity field, to constrain, among other things, basal sliding. We introduce two different approaches of combining a physical parameter, the basal roughness, with basal sliding parametrisations. This way basal sliding is connected again closer to its original formulation. We show that the basal roughness is an important and helpful parameter to consider and that many features of the flow structure can be reproduced with these approaches.

1 Introduction

In the past decades the fastest changes in ice flow velocity, ice thickness and grounding line retreat in the Antarctic Ice Sheet have been observed in the region of Pine Island Glacier (PIG), Amundsen Sea Embayment, West Antarctica (Rignot, 2008; Wingham et al., 2009; Rignot, 1998; Joughin et al., 2010; Park et al., 2013). Additionally, the currently observed mass loss from the Antarctic Ice Sheet is also concentrated in the area around PIG (Horwath and Dietrich, 2009; Shepherd et al., 2012). Thus PIG shows an increased contribution to global sea level rise (Mouginot et al., 2014).

The bed below PIG lies below sea level in large areas, making it part of a so called marine ice sheet. In combination with a retrograde bed, which slopes down from the ocean towards the center of the glacier, this setting was postulated to be intrinsically unstable, via the so called "Marine Ice Sheet Instability" hypothesis (Hughes, 1973). This hypothesis is still up

for debate (Vaughan, 2008; Gudmundsson et al., 2012), while the trigger for the changes is thought to be enhanced ocean melting of the ice shelf (Dutrieux et al., 2014).

The dynamics of PIG are crucial for its future behaviour and therefore for its contribution to sea level rise. An important tool for investigating glacier dynamics are numerical ice flow models. Ice flow models simulate the flow of glacier ice, which is due to a combination of internal deformation and basal motion. Depending on the subglacial setting, basal motion can dominate the overall motion of a glacier, which is also the case for large areas of PIG. The parametrisation of basal motion in ice flow models is therefore important for the overall dynamics of a glacier. On the other hand the difficulty of observing basal properties renders the parametrisation one of the most challenging parts in ice flow modelling. In the absence of information on basal properties like bed type, structure and availability of liquid water, control methods are applied to simulate a complex glacier flow pattern, as present at PIG (e.g. MacAyeal, 1992; Joughin et al., 2009, 2010; Morlighem et al., 2010; Favier et al., 2014). These methods use the measured surface velocity field to invert for basal properties or effective viscosity and to adjust basal sliding parameters. Depending on the focus of the study, these approaches can provide important insights into glacier dynamics.

Due to the fast changes observed at PIG, a variety of modelling studies have been conducted on it. These studies address questions focusing on the sensitivity to changes in external conditions (ice shelf buttressing, basal conditions) (e.g. Schmelz et al., 2002) and on the contribution to future sea level rise (e.g. Joughin et al., 2010). The overarching question is, if the system will stabilise again in the near future, or if retreat might even accelerate (e.g. Katz and Worster, 2010; Gladstone et al., 2012; Favier et al., 2014; Seroussi et al., 2014).

The question whether the system will stabilise again in the future is an important one to address. Nonetheless in modelling studies one needs to simplify things, being forced to focus on certain processes and neglect others. The prognostic studies on PIG all use control methods to constrain basal sliding. Thus they define a spatially varying basal sliding parameter for the present flow state, and keep it constant during the prognostic simulations. This way the basal sliding system is somehow decoupled from the rest of the system. Changes

in basal conditions, by for example subglacial erosion (Smith et al., 2012; Rippin et al., 2014) or dynamic hydraulic systems, can not be considered with this approach. However, the basal sliding behaviour might be the crucial process to cause a further retreat or halt of the system. Gudmundsson et al. (2012) show that stable grounding line positions can be found on a retrograde bed, using models with 2 horizontal dimensions. We believe the basal sliding behaviour is a similarly important process as is the lateral buttressing. Therefore we focus on basal sliding parametrisations that consider measured basal roughness distributions. This accessible bed information could be in further steps combined with for example a time-dependent hydrological model, to consider changing basal conditions for the sliding behaviour of the glacier.

Here we present results of the thermo-mechanical 3D full-Stokes model COMice (implemented in the COMmercial finite element SOLver COMSOL Multiphysics[®], cf. Pattyn et al. (2013); Wilkens (2014)), applied diagnostically to PIG. Initially we conduct a diagnostic inversion for a basal sliding parameter, as done in previous studies, to generate a reference simulation and analyse the thermal structure of the glacier. Since the inversion for basal sliding parameters is not sufficient for the physical understanding of basal motion, we introduce and test in a second step two methods of connecting basal roughness measures to the parametrisation of basal sliding and therefore constrain basal sliding with physically justified assumptions. Additionally we couple the sliding behaviour to the basal temperature, adding another physically based constraint. The first method matches a single-parameter basal roughness measure for PIG, as presented in Rippin et al. (2011), onto a basal sliding parameter. The second method is based on ideas from Li et al. (2010), where we use a two-parameter basal roughness measure, especially calculated for this study, to connect basal roughness to basal sliding. The results are subsequently analysed and discussed.

2 The numerical flow model

2.1 Governing equations

The governing equations for the thermo-mechanical ice flow model COMice are the fluid dynamical balance equations, together with a formulation for the non-Newtonian rheology of ice. The balance equations are set up for mass, momentum and energy, and solved for the velocity vector \mathbf{u} , the pressure p and the temperature T .

The mass balance equation is given in case of incompressibility as

$$\operatorname{div} \mathbf{u} = 0. \quad (1)$$

The momentum balance equation is the Stokes equation, given by

$$\operatorname{div} \boldsymbol{\sigma} = -\rho_i \mathbf{g}, \quad (2)$$

with the Cauchy stress tensor $\boldsymbol{\sigma}$, the density of ice ρ_i and the acceleration of gravity $\mathbf{g} = (0, 0, -g)^T$. The stress tensor $\boldsymbol{\sigma}$ is split into a velocity dependent part $\boldsymbol{\tau}$, the deviatoric stress, and a pressure dependent part $p\mathbf{I}$, with the identity matrix \mathbf{I} , such that $\boldsymbol{\sigma} = \boldsymbol{\tau} - p\mathbf{I}$. For incompressible materials only the deviatoric stress $\boldsymbol{\tau}$ can result in strains, and is thus related to the velocity field \mathbf{u} , via the strain-rate tensor $\dot{\boldsymbol{\epsilon}}$ and the ice viscosity μ , such that $\boldsymbol{\tau} = 2\mu\dot{\boldsymbol{\epsilon}}$. The strain-rate tensor $\dot{\boldsymbol{\epsilon}}$ is given in components as

$$\dot{\epsilon}_{ij} = \frac{1}{2} \left(\frac{\partial u_i}{\partial x_j} + \frac{\partial u_j}{\partial x_i} \right),$$

in relation to Cartesian basis vectors. The ice viscosity μ is described with use of Glen's flow law (Glen, 1955; Nye, 1957), such that

$$\mu(T', \dot{\boldsymbol{\epsilon}}_e) = \frac{1}{2} [A(T')]^{-1/n} \dot{\boldsymbol{\epsilon}}_e^{\frac{1-n}{n}}, \quad (3)$$

with the rate factor $A(T')$, the stress exponent n and the effective strain rate

$$\dot{\epsilon}_e = \sqrt{\frac{1}{2} \text{tr}(\dot{\epsilon}^2)}, \quad (4)$$

which is a scalar invariant of the strain-rate tensor $\dot{\epsilon}$. The viscosity μ depends on the homologous temperature T' and the effective strain rate $\dot{\epsilon}_e$. The homologous temperature T' is the temperature relative to the pressure melting point T_{pmp} , defined as

$$T' = T + \beta_c p, \quad (5)$$

with the Clausius-Clapeyron constant β_c .

The pressure melting point T_{pmp} is described for typical pressures in ice sheets ($p \lesssim 50$ MPa) by a linear relation, such that

$$T_{\text{pmp}} = T_0 - \beta_c p, \quad (6)$$

with the melting point at low pressures T_0 .

The rate factor $A(T')$ parametrises the influence of the temperature and the pressure onto the viscosity μ and is described by $A(T') = A_0 e^{-Q/RT'}$ (Greve and Blatter, 2009), with a pre-exponential constant A_0 , the activation energy for creep Q and the gas constant R .

The energy balance equation is given as

$$\rho c_p(T) \left(\frac{\partial T}{\partial t} + \mathbf{u} \text{ grad } T \right) = \text{div}(\kappa(T) \text{ grad } T) + \psi, \quad (7)$$

with the thermal conductivity $\kappa(T)$, the specific heat capacity $c_p(T)$ and an internal heat source term $\psi = 4\mu\dot{\epsilon}_e^2$, which connects mechanical and thermal energy.

The scalar values for all parameters used throughout this study are listed in Table 1.

2.2 Boundary conditions

The balance equations are defined under the assumption that the thermodynamic fields are sufficiently smooth, thus continuously differentiable, which is only the case for the inner parts of the glacier. The outer boundaries need specifically formulated boundary conditions.

5 The vertical boundaries are the upper surface z_s and the base z_b of the glacier. The lateral boundaries are given by the ice divide, an inflow area and the calving front, indicated in Fig. 1. The grounding line indicates the change of the basal boundary conditions from grounded to floating ice.

2.2.1 Mass

10 Since the model is applied in a diagnostic manner and therefore the geometry is fixed, only the ice base z_b needs a kinematic boundary condition, to prevent the flow to point into the ground, and is given as $\mathbf{u} \cdot \mathbf{n} = 0$, with the unit normal vector \mathbf{n} pointing outwards from the surface. This formulation is applied to the entire ice base z_b , including grounded and floating parts, and also implies that no basal melting is considered.

2.2.2 Stress

15 The upper surface z_s can be seen to be traction free by assuming that wind stress and atmospheric pressure are negligible compared to the typical stresses in the ice sheet, such that $\boldsymbol{\sigma} \cdot \mathbf{n} = 0$.

At the base of the floating ice shelf shear stress induced by circulating sea water can be neglected (Weis et al., 1999) and the only stress onto the ice is exerted by the water. As the ice shelf floats it is assumed to fulfil the floating condition and the stress applied equals the stress of the displaced water column (Greve and Blatter, 2009), such that $\boldsymbol{\sigma} \cdot \mathbf{n} = -\rho_{sw} g (z_{sl} - z_b) \cdot \mathbf{n}$, with the density of sea water ρ_{sw} and the mean sea level z_{sl} .

20 For the boundary condition of the grounded ice, it is assumed that the stress vector $\boldsymbol{\sigma} \cdot \mathbf{n}$ is continuous across the interface, such that $\boldsymbol{\sigma} \cdot \mathbf{n} = \boldsymbol{\sigma}_{lith} \cdot \mathbf{n}$, with the Cauchy stress tensor of the lithosphere $\boldsymbol{\sigma}_{lith}$. Since this tensor is not known, the condition has to be approximated.

This is done with a sliding law that connects the basal sliding velocity $\mathbf{u}_b = (\mathbf{u} \cdot \mathbf{t}_x, \mathbf{u} \cdot \mathbf{t}_y)^T$, with the unit tangential vectors \mathbf{t}_x in the xz -plane and \mathbf{t}_y in the yz -plane, to the basal drag $\boldsymbol{\tau}_b = ((\boldsymbol{\sigma} \cdot \mathbf{n}) \cdot \mathbf{t}_x, (\boldsymbol{\sigma} \cdot \mathbf{n}) \cdot \mathbf{t}_y)^T$. In its simplest form it can be written as a linear connection, such that

$$5 \quad \boldsymbol{\tau}_b = \beta^2 \mathbf{u}_b, \quad (8)$$

where β^2 is a basal sliding parameter including all factors influencing the basal sliding behaviour other than the linear connection to basal stress. A more detailed description of sliding laws can be found in Sect. 3.2, as they are of central interest for this study.

10 Ice divides can be seen as mirror points where the direction of the driving stress and flow on one side of the divide opposes that of the other side. No flow across the ice divide is allowed, the tangential stresses vanish and therefore the boundary condition for ice divides is given by

$$\mathbf{u} \cdot \mathbf{n} = 0 \quad , \quad (\boldsymbol{\sigma} \cdot \mathbf{n}) \cdot \mathbf{t}_x = 0 \quad \text{and} \quad (\boldsymbol{\sigma} \cdot \mathbf{n}) \cdot \mathbf{t}_y = 0. \quad (9)$$

The boundary condition at the calving front is given by

$$15 \quad \boldsymbol{\sigma} \cdot \mathbf{n} = -p_{sw} \mathbf{n}, \quad (10)$$

with the water pressure p_{sw} defined as

$$p_{sw} = \begin{cases} 0 & \text{for } z \geq z_{sl} \\ \rho_{sw} g (z_{sl} - z) & \text{for } z < z_{sl}. \end{cases} \quad (11)$$

The boundary condition for the inflow region is given as a Dirichlet condition by an inflow velocity field defined with the Shallow Ice Approximation (Hutter, 1983; Morland, 1984).

20 2.2.3 Temperature

The boundary conditions for the upper surface z_s and the ice shelf base, which is only the floating part of z_b , are given by Dirichlet conditions in prescribing the average annual surface temperature $T_s(x, y, t)$ and the freezing temperature of seawater T_{sw} , respectively.

At the base of the grounded ice the boundary condition has to be formulated as a Neumann condition and the temperature gradient is prescribed as

$$\text{grad} T \cdot \mathbf{n} = \frac{q_{\text{geo}} + q_{\text{fric}}}{\kappa(T)}, \quad (12)$$

with the geothermal heat flux q_{geo} and the friction heating term $q_{\text{fric}} = \mathbf{u}_b \cdot \boldsymbol{\tau}_b$ (Pattyn, 2003).

5 This condition is only valid as long as $T \leq T_{\text{pmp}}$. If the basal temperature T reaches the pressure melting point T_{pmp} , it has to be switched to a Dirichlet condition with $T = T_{\text{pmp}}$, as the ice can not become warmer.

The boundary condition for the ice divide and the calving front are based on the assumption that there is no temperature gradient across the surface. It can thus be written in form
10 of a thermal insulation $(\kappa(T) \text{grad} T) \cdot \mathbf{n} = 0$.

Temperatures at the inflow boundary are prescribed by a linear profile $T_{\text{lin}} = \frac{T_{\text{pmp}} - T_s}{z_s - z_b} (z_s - z) + T_s$.

2.3 Implementation

The thermo-mechanically coupled 3D full-Stokes model COMice is implemented in the
15 COMmercial finite element SOLver COMSOL Multiphysics[®] (cf. Wilkens (2014) for implementation details). The model has been successfully applied in the diagnostic tests in the MISMIP 3D model intercomparison project (Pattyn et al., 2013).

2.3.1 Ice flow model

The ice flow model solves for the the velocity vector \mathbf{u} and the pressure p . The Babuska-
20 Brezzi condition requires for numerical stability, that the basis functions for p are of lower order than for \mathbf{u} . Therefore we use linear elements for p and quadratic elements for \mathbf{u} (P1+P2).

To the effective strain rate $\dot{\epsilon}_e$ (Eq. (4)) a small value of 10^{-30} s^{-1} is added, to keep the term non-zero. Model experiments have shown, that this does not affect the overall results
25 (Pattyn, 2003; Cornford et al., 2012).

The boundary conditions set in the ice flow model are the kinematic and dynamic ones stated in Sect. 2.2.1 and 2.2.2, respectively. The kinematic condition at the ice base is implemented as a weak constraint, for stability reasons. Weak constraints apply boundary conditions in an integral sense and are therefore not as strict. They stand in contrast to pointwise constraints, which force the nodal value to the constraint and can thus lead to numerical instability (COMSOL, 2012).

The basal stress vector is implemented consisting of its tangential part (Eq. (8)) and a normal part, given by the effective normal stress N_b (Eq. (15)), further described in Sect. 3.2, such that

$$\boldsymbol{\sigma} \cdot \mathbf{n} = \beta^2 u_b \mathbf{t}_x + \beta^2 v_b \mathbf{t}_y - N_b \mathbf{n}, \quad (13)$$

with $u_b = \mathbf{u} \cdot \mathbf{t}_x$ and $v_b = \mathbf{u} \cdot \mathbf{t}_y$.

To the outer wall of the ice rises a no slip condition is assigned, as they are implemented as holes in the geometry.

2.3.2 Thermal model

The temperature is discretized with linear elements, with boundary conditions from Sect. 2.2.3.

To avoid numerical instabilities due to strong temperature advection, and thus to ensure that the element Péclet number is always < 1 , we use consistent stabilization methods provided by COMSOL Multiphysics[®]. Equation 7 is solved using a Galerkin Least Square (GLS) formulation (Codina, 1998) in streamline direction and crosswind diffusion (Hauke and Hughes, 1998) orthogonal to the streamline direction. The chosen stabilization methods add less numerical diffusion the closer the numerical solution comes to the exact solution (COMSOL, 2012).

All Dirichlet conditions for the thermal model are implemented as weak constraints, for stability reasons.

The Neumann condition for the temperature at the base z_b is implemented in a way, that a heat flux is prescribed, as long as $T < (T_{b,\max} - 0.01)$. The expression $T_{b,\max}$ prescribes

a spatially variable field that defines the maximal basal temperature allowed for a region (T_{pmp} for grounded areas, T_{sw} for floating areas). If $T \geq (T_{\text{b,max}} - 0.01)$, the heat flux is gradually reduced and turns zero when $T = (T_{\text{b,max}} + 0.01)$. This procedure ensures that the basal heat flux can not increase T_{b} above $T_{\text{b,max}} + 0.01$. The smoothing of the step function ensures numerical stability, which was not found with a sharp step.

2.3.3 Mesh

To maximise the resolution while minimising the amount of elements, we use an unstructured finite element mesh, shown in Fig. 2. The upper surface z_s is meshed first with triangles. The horizontal edge lengths are 5 – 500 m at the grounding line and the calving front, 50 – 1000 m at the inflow area and 100 – 2000 m at the rest of the outer boundary. The resulting 2D surface mesh is extruded through the glacier geometry with a total of 12 vertical layers everywhere. The thickness of the vertical layers varies only with ice thickness. The spacing between the layers is refined towards the base. The ratio of the lowest to the upper most layer thickness is 0.01, leading to a thickness of the lowest layer of about 5 m for a total ice thickness of 3000 m. The final mesh consists of $\sim 3.5 \times 10^5$ prism elements, which results in $\sim 5 \times 10^6$ degrees of freedom (DOF), when solved for all variables.

2.3.4 Solver

For solving the nonlinear system, a direct segregated solver is used, which conducts a quasi-Newton iteration. It solves consecutively: first for the velocity \mathbf{u} and the pressure p , and thereafter for the temperature T (COMSOL, 2012). This allows for reduced working memory usage. For the remaining linear systems of equations the direct solver Pardiso (COMSOL (2012) and <http://www.pardiso-project.org/>, last access: 9 December 2014) is applied. While uncommon for such large numbers of DOF's, it proved to be computationally viable and robust, since all available iterative solvers exposed instabilities on this problem.

2.3.5 Geometry and input data

The geometry of the model was built with a consistent set of surface elevation, ice thickness and bed topography on a 1 km grid, created by A. Le Brocq and kindly provided by her for this work. The data set represents the thickness distribution of PIG for the year 2005 and earlier. The Le Brocq data are based on the surface elevation data of Bamber et al. (2009) and the ice thickness data of Vaughan et al. (2006).

The grounding line position used is given by a combination of the positions in the MODIS Mosaic Of Antarctica (MOA, Bohlander and Scambos, 2007), corresponding to the years 2003/2004, the position in Rignot (1998), corresponding to 1996, and the position that gives the smoothest ice thickness join of the glacier geometry, assuming the floatation condition. The location of the ice rises pinning the ice shelf at present are detected on TerraSAR-X images from 2011, with assistance of interferograms from Rignot (2002). The surface temperature used here is on a 5 km grid compiled by Le Brocq et al. (2010) (ALBMAP v1), based on the temperature data described in Comiso (2000). We use the geothermal heat flux q_{geo} from 2012 (updated version of Fox Maule et al., 2005), because a variety of sensitivity tests showed, that other data sets lead to too high velocities in regions with no or little basal sliding. The observed surface velocity is taken from Rignot et al. (2011), shown in Fig. 1, and used to validate the reference simulation.

3 Methods: roughness data and sliding laws

The central focus of this study is to investigate how basal sliding and measured basal roughness could be connected in a formulation of a basal sliding law. We will therefore first describe the roughness data used throughout this study. Thereafter we will give an overview of the basal sliding laws used and elucidate their connection to basal properties.

3.1 Roughness data

In this study we use two different data sets of basal roughness measures, compiled for the base of PIG. The first one is the single-parameter roughness measure as presented in Rippin et al. (2011) (c.f. Fig. 4b therein). The second one is a two-parameter roughness measure calculated especially for this study along ideas from Li et al. (2010).

Both roughness measures are based on Fourier transformations (FT), which is a key technique to derive basal roughness. A FT can be used to transform any surface into a sum of several periodically undulated surfaces. This way the amplitude and spatial frequency of the undulations can be expressed. For theoretical dynamic studies characterising the roughness by FT works well. However, to show the spatial distribution of roughness, in a glaciological context, a single-parameter measure ξ was introduced (Hubbard et al., 2000; Taylor et al., 2004). The single-parameter roughness measure ξ is defined as the integral of the spectrum within a specified wavelength interval. This method represents the amplitude of the undulations, but information about the frequency is lost. For PIG the single-parameter roughness measure ξ was calculated by Rippin et al. (2011) from a RES data set generated in austral summer 2004/05 (Vaughan et al., 2006). It is the same data set the model geometry is based on (Sect. 2.3.5), still the roughness measure includes higher resolution information, as the derivation is based on along track sample spacing of the order of 30 m (cf. Rippin et al. (2011)). Both data sets are then gridded with 1 km spacing.

Li et al. (2010) introduce a two-parameter roughness measure that represents the amplitude ξ_2 and frequency η_2 of the undulations. They introduce an interpretation how different basal topographies with their geomorphic implications can be distinguished from patterns of ξ_2 and η_2 . The interpretation from Li et al. (2010) is based on ideas by Bingham and Siegert (2009), which give an interpretation for the single-parameter roughness. Rippin et al. (2014) extended the interpretation for the two-parameter roughness measure. The implications for PIG will be discussed below.

Because of the statistical meanings of ξ_2 and η_2 , they can be used as representatives for the vertical and horizontal length scales present at the base. To do so the integration interval for $\{\xi_2, \eta_2\}$ should be in the metre-scale waveband (Li et al., 2010).

The two-parameter roughness measure for PIG was calculated for this study. The spatial resolution of the underlain data for PIG is 34 m. A moving window is calculated with ($N = 5$, $2^N = 32$), which is the minimum for N that should be used (e.g. Taylor et al., 2004). With a spatial resolution of 34 m this leads to a moving window length of 1088 m, which is in the metre-scale waveband required by Li et al. (2010), to be able to apply the data in a sliding relation. The received fields of ξ_2 and η_2 for PIG are shown in Fig. 3.

According to Li et al. (2010), different basal properties and related geomorphic implications can be distinguished from patterns of ξ_2 and η_2 . A marine setting with intensive deposition and fast and warm ice flow, as proposed for the central part of PIG, is characterised by low values of ξ_2 and high values of η_2 , thus low-amplitude, low-frequency roughness.

Here it has to be noted that the second parameter η_2 should be more accurately seen as representing the wavelength of roughness, rather than the frequency, as high values correspond to low frequencies (Rippin et al., 2014). Nonetheless we continue here referring to η_2 as the roughness frequency for consistency with Li et al. (2010).

The suspected low-amplitude, low-frequency roughness is not necessarily found in the central trunk area, as can be seen in Fig. 3. Instead it seems to be more dominated by low-amplitude, high-frequency roughness, which can, following Li et al. (2010), be interpreted as a continental setting after intensive erosion, also with fast and warm ice flow. Still, this interpretation can not be seen as a contradiction to the suspicion of the presence of marine sediments. It is important to state that absolute values of roughness cannot be derived from these calculations, but rather it is the patterns relating to relative roughness values that are significant.

3.2 Sliding laws

So called "Weertman-type sliding laws" are most commonly applied in modern modelling studies, for which the basis was established by Weertman (1957). He developed a mathe-

mathematical description for the mechanisms that influence basal sliding. One focus lay hereby on connecting small scale processes with larger scale sliding effects. Nye (1969) and Kamb (1970) worked on related problems and they all found that the basal sliding velocity u_b varies with some power of the basal shear stress τ_b , depending on the dominant mechanism. Additionally they find that the basal sliding velocity u_b also sensitively depends on the roughness of the bed.

The processes considered by Weertman (1957), Nye (1969) and Kamb (1970) are only relevant for sliding over hard bedrock, where an upper limit for sliding velocities is found ($u_b < 20 \text{ m a}^{-1}$ Cuffey and Paterson (2010)). For faster sliding velocities weak deformable substrate or water filled cavities have to be present. Water filled cavities reduce the contact between the ice and the bedrock, therefore effectively reducing the roughness of the bed and their effect can be considered via the basal normal stress N_b , also called effective pressure (Bindschadler, 1983).

Fast sliding velocities can only occur when the glacier base is at pressure melting point, but also below these temperatures some sliding can be present (Fowler, 1986). This mechanism can be reflected by a temperature function $f(T)$, which regulates sub-melt sliding.

Considering the above stated thoughts leads to a sliding law of the form

$$u_b = C_b |\tau_b|^{p-1} N_b^{-q} f(T) \tau_b = \frac{1}{\beta^2} \tau_b, \quad (14)$$

whereby C_b is originally seen as a roughness parameter, p and q are basal sliding exponents and N_b is related to the basal normal stress, defined in Eq. (15). When written in a linearised form, as already introduced in Sect. 2.2.2, all effects influencing the basal sliding velocity u_b , other than the linear relation to the basal shear stress τ_b , are summerized in a basal sliding parameter β^2 , which leads to a spatially varying field obtained by inversion techniques.

In the following we will further define the single components in the basal sliding law, as used throughout this study.

The basal normal stress N_b is a vector of the form $N_b = -N_b \mathbf{n}$. The overburden pressure of the ice is reduced in marine parts by the uplifting water pressure (Huybrechts, 1992),

such that

$$N_b = \begin{cases} \rho_i g H & \text{for } z_b \geq z_{sl} \\ \rho_i g H + \rho_{sw} g z_b & \text{for } z_b < z_{sl}, \end{cases} \quad (15)$$

with the ice thickness H . The assumptions made above imply a hydrology network which is perfectly connected to the ocean. This assumption is plausible near the grounding line, but becomes highly speculative towards the marine regions further inland. An additional hydrological model would be needed to realistically simulate the effective basal pressure, but is beyond the scope of this study. Even though more sophisticated parametrisations for the effective pressure exist (e.g. Leguy et al. (2014)), we stick with the strong assumption stated above, as water is likely present below all fast flowing parts of PIG (Smith et al., 2013), which coincide with the marine regions.

The temperature function $f(T)$ is taken as suggested by Budd and Jenssen (1987) as an exponential function, such that

$$f(T) = e^{\nu(T-T_{\text{mp}})}, \quad (16)$$

with a submelt sliding parameter ν .

The roughness parameter C_b will be related to the single-parameter roughness measure from Rippin et al. (2011) in Sect. 4.2, and described in detail there.

A different approach to describe basal sliding, and also considered in this study, is introduced by Li et al. (2010). It is based on Weertmans original formulation (Weertman, 1957) of describing the sliding mechanisms of regelation and enhanced creep, such that

$$u_b = C_W \left(\tau_b \frac{l^2}{a^2} \right)^{\frac{(1+n)}{2}}, \quad (17)$$

whereby C_W is a parameter defined by thermal and mechanical properties of the ice ($C_W = 4.46 \times 10^{-29} \text{ m}^3 \text{ s}^3 \text{ kg}^{-2}$, in our example), l is the obstacle spacing, a the obstacle size (cf. Weertman (1957)) and $n = 3$ the stress exponent.

Li et al. (2010) state that the two-parameter roughness measures ξ_2 and η_2 , representing the amplitude and frequency of the roughness (cf. Sect. 3.1), can be used as a proxy for the vertical and horizontal length scales present at the base, due to their statistical meanings, such that

$$5 \quad a = c_1 \xi_2^{\frac{1}{2}} \quad \text{and} \quad l = c_2 \eta_2^{\frac{1}{2}},$$

with c_1 and c_2 being proportionality factors.

Entering this into Weertmans original formulation (Eq. (17)) and additionally including a temperature function $f(T)$ as introduced above, leads to

$$10 \quad u_b = C_L f(T) \left(\tau_b \frac{\eta_2}{\xi_2} \right)^{\frac{(n+1)}{2}}, \quad (18)$$

with the constant $C_L = C_W (c_2/c_1)^{1+n}$. As the proportionality factors c_1 and c_2 are not further defined, we take C_L as a single parameter to adjust.

4 Results

We conduct numerical simulations with the model COMice set up for the PIG region. First, in Sect. 4.1, a reference simulation is conducted, where measured surface velocities are inverted for basal sliding parameters, as is commonly done for modelling the flow of PIG (e.g. Joughin et al., 2009; Morlighem et al., 2010; Favier et al., 2014; Seroussi et al., 2014). This approach leads to a realistic surface flow structure and lets us analyse the thermal structure of the glacier. Nonetheless the approach is dissatisfying when aiming to constrain basal sliding with physical parameters at the base of the glacier. Therefore, in a second step, we introduce two approaches for the parametrisation of basal sliding that consider the basal roughness below the glacier in the formulation of a basal sliding law. The first approach, Sect. 4.2, is based on the Weertman-type sliding law as shown in Eq. (14) and considers the single-parameter roughness measure from Rippin et al. (2011). The second

approach, Sect. 4.3, is based on the idea of Li et al. (2010) to connect basal sliding to the two-parameter roughness measure, introduced in Sect. 3.1.

4.1 Reference Simulation

The main difficulty is to capture the distinct surface flow pattern, by making appropriate assumptions about the basal sliding behaviour. Many ice modelling studies use a constant set of basal sliding parameters to reproduce somewhat realistic surface velocity fields (e.g. Rückamp, 2011; Kleiner and Humbert, 2014). This approach can not be adopted for PIG, as it leads to a shut down of parts of the fast flowing main trunk, due to very low basal shear stresses in that region (Joughin et al., 2009; Morlighem et al., 2010). Instead, for our reference simulation, an inversion for basal parameters is conducted, as already done by previous studies (e.g. Joughin et al., 2009; Morlighem et al., 2010; Favier et al., 2014).

4.1.1 Simulation procedure

The inversion method (cf. Schmeltz et al., 2002) used for our reference simulation starts by assuming a linear sliding law of the form $\tau_b = \beta^2 \mathbf{u}_b$ (inverted version of Eq. (14)), with β^2 being the basal sliding parameter to be inferred.

Additionally a simulation is conducted, where the glacier base is not allowed to slide. Therefore the resulting surface velocity field $\mathbf{u}_{s,\text{nosl}}$ can be seen to be solely due to internal deformation. The basal sliding velocity \mathbf{u}_b can be approximated by subtracting the surface velocity due to internal deformation $\mathbf{u}_{s,\text{nosl}}$ from the measured surface velocity field \mathbf{u}_{obs} (Rignot et al. (2011), Fig. 1). The basal drag from the simulation where no basal sliding is allowed $\tau_{b,\text{nosl}}$ is taken as a good first representative of the real basal drag distribution τ_b . With this the field of the basal sliding parameter β^2 is defined as

$$\beta^2 = |\tau_{b,\text{nosl}}| (|\mathbf{u}_{\text{obs}}| - |\mathbf{u}_{s,\text{nosl}}|)^{-1}, \quad (19)$$

shown in Fig. 4.

The basal sliding parameter β^2 is subsequently applied in the forward model in the linear sliding law. Since the amount of internal deformation in the ice crucially depends on the ice

temperature (Eq. (3)), it is important to consider a realistic temperature distribution within the ice. At this point it is important to note, that the model is applied in a diagnostic manner and therefore the received temperature distribution is a steady state one for a fixed geometry with constant boundary conditions, which might differ from the actual transient field.

5 Nonetheless the received field is likely to show a better approximation to reality than simply assuming a certain distribution. To consider a realistic temperature distribution within the ice, we conduct the above described procedure in an iterative manner. We first conduct a “no sliding” simulation $\text{nosl}, 1$, with a constant temperature of $T = 263.15\text{K}$. The resulting surface velocity field $\mathbf{u}_{\text{s,nosl},1}$ and basal drag $\tau_{\text{b,nosl},1}$ lead to a basal sliding parameter β_1^2 .

10 This basal sliding parameter β_1^2 enters the simulation with basal sliding $\text{sl}, 1$, where the temperature field is now solved for as well. The thus found temperature distribution enters the next “no sliding” simulation $\text{nosl}, 2$ as a constant field. Now again a basal sliding parameter β_2^2 is found, entering the next simulation with basal sliding $\text{sl}, 2$, which is our final reference simulation, later referred to as ref . Thus the procedure is stopped after two

15 iterations, and listed in a schematic manner as: $\text{nosl}, 1(T = 263.15\text{K}) \rightarrow \beta_1^2 \rightarrow \text{sl}, 1(T \text{ solved}) \rightarrow \text{nosl}, 2(T \text{ from } \text{sl}, 1) \rightarrow \beta_2^2 \rightarrow \text{sl}, 2/\text{ref}(T \text{ solved})$.

4.1.2 Velocity field

The resulting surface velocity field from the reference simulation is shown in Fig. 5, together with an indication and numbering of the different tributaries, feeding into the fast flowing central stream.

20 The numbering of the tributaries for tributaries 1-10 is based on Stenoien and Bentley (2000). The numbering used in Vaughan et al. (2006), Karlsson et al. (2009) and Rippin et al. (2011) is the same for the even numbers, but shifted by 1 for the odd numbers, as they missed tributary 1 from the numbering by Stenoien and Bentley (2000). We extended the numbering from Stenoien and Bentley (2000) to the tributaries 11-14,

25 which are entering the ice shelf.

The general pattern of the surface velocity field is well reproduced in the reference simulation, compared to the observed surface velocity field $|\mathbf{u}_{\text{obs}}|$ (Rignot et al., 2011, shown in Fig. 1). The tributaries are all in the right location and the velocity magnitudes agree in most

areas well. The highest differences between $|\mathbf{u}_{s,\text{ref}}|$ and $|\mathbf{u}_{\text{obs}}|$ are found in the ice shelf, where the simulated velocities are up to 1 km a^{-1} smaller than the observed ones.

When solely looking at the velocity magnitudes, shown in Fig. 6, we again find that for higher velocities the simulated velocity field $|\mathbf{u}_{s,\text{ref}}|$ is lower than the observed field $|\mathbf{u}_{\text{obs}}|$.

5 The spread around the diagonal for lower velocities appears bigger, which is mainly due to the logarithmic axes chosen. For higher flow velocities the direction of flow of the simulated field agrees well to the direction of the observed field. This is shown as a colour code for the angle offset between the velocity vectors in Fig. 6. For slower velocities the angle offset is bigger, coinciding with a higher measurement error for slower velocities.

10 4.1.3 Temperature regime

Our simulations show, that under PIG large areas are at the pressure melting point T_{pmp} . This can be seen in Fig. 7, where the temperature relative to the pressure melting point at the base $T'_{\text{b,ref}}$ (homologous temperature as given in Eq. (5)), is shown. In general the overall flow pattern is reflected in the basal temperature structure, with fast flowing areas
15 being underlain by a temperate base. This can be seen with help of the location of the tributaries in Fig. 7.

Figure 8 shows the homologous temperature T'_{ref} at three vertical slices, of which the location is indicated in Fig. 7. The first slice shown in Fig. 8a is located furthest away from the ice shelf, towards the inner parts of the glacier. Figures 7 and 8 show that the base is mainly temperate while the inner ice body, away from the base, is predominantly cold. A
20 similar picture is found in the next slice, shown in Fig. 8b, which is located further downstream towards the ice shelf. Here, additionally a cold core can be seen, located in the fast flowing central stream (cf. Fig. 5). The next slice, shown in Fig. 8c, partly crosses the ice shelf. It can be well observed that a cold core is entering the ice shelf. To the right of the
25 ice shelf, approximately where tributary 11 is located (cf. Fig. 7), a small temperate layer is found.

4.2 Parametrisation 1: Relating the single-parameter roughness measure ξ to the basal sliding parameter C_b

4.2.1 Simulation procedure

From the results of the reference simulation, it could be suspected that different types of sliding conditions must be present below PIG. Instead of inverting for one spatially varying parameter, we now connect the basal sliding parameter C_b of Eq. (14) to the measured basal roughness ξ (Rippin et al. (2011), Sect. 3.1), as it is closest to the originally physical meaning of C_b (cf. Sect. 3.2).

In the following we will refer to the basal sliding parameter C_b , when it is related to the basal roughness measure ξ in this section as C_ξ . The absolute values of the roughness measure ξ are dependent on parameters chosen for its derivation. At the same time the sliding parameter C_b depends not only on mechanical properties, such as basal roughness, but also thermal properties. Therefore, the roughness measure ξ can not directly be used as the sliding parameter C_ξ .

To use the roughness information, we select a range for the sliding parameter C_b , obtained via the approximation

$$C_b = \frac{(|\mathbf{u}_{\text{obs}}| - |\mathbf{u}_{\text{s,nosl}}|) N_b^q}{|\boldsymbol{\tau}_{\text{b,nosl}}|^p}, \quad (20)$$

with the effective normal stress N_b (Eq. (15)) and $p = 1$. The basal sliding exponent q is taken as 0, 1 or 2, which regulates the effect of the effective normal stress onto the sliding velocities. The resulting logarithmic range is thereafter matched onto the normed and inverted distribution of the roughness measure ξ . It is inverted as lowest roughness correlates with highest basal sliding and therefore highest values of C_ξ . This way we make sure to derive surface velocities within a realistic range.

We conduct 15 simulations, where each parameter combination represents a potential subglacial setting. In all simulations $p = 1$, while q is varied. Simulations 1-5 are conducted with $q = 0$, simulations 6-10 with $q = 1$ and simulations 11-15 with $q = 2$. For the different

values of q , the range of C_ξ is varied. The widest range of C_ξ consists of the maximum values found by approximation for C_b (Eq. (20)). Exact values can be found in (Wilkins, 2014).

4.2.2 Velocity field

- 5 The resulting surface velocity fields are analysed in a quantitative and qualitative manner. For the quantitative manner the root-mean-square (RMS) deviation RMS_{u_s} between the simulated and the reference surface velocity fields are analysed. The RMS_{u_s} is given by

$$\text{RMS}_{u_s} = \sqrt{\frac{1}{m} \sum_{i=1}^m (|\mathbf{u}_{s,\text{sim}}|_i - |\mathbf{u}_{s,\text{ref}}|_i)^2}, \quad (21)$$

with m being the number of discrete values on a regular grid with 1 km spacing.

- 10 The surface flow field is additionally separated into three distinct regions of fast flow velocities ("Fast"), slower flow velocities ("Slow") and the entire model region ("All") (detailed description in Wilkins (2014)). The regions of all tributaries (1-14), the central stream (CS) and the shelf area (Shelf), as shown in Fig. 9b and 9c, are combined to the region "Fast", while the remainder is the region "Slow".

- 15 Figure 9a shows the RMS_{u_s} for the regions "Fast", "Slow" and "All" between the simulated and the reference surface velocity fields. It can be seen, that the "Fast" regions differ most for all parameter combinations tested here. Additionally for the entire region "All" there seems to be no single parameter combination, that minimises the RMS_{u_s} value and therefore appropriately represents the basal conditions below PIG in a sliding law. Nonetheless
 20 some of the complex surface flow features could be reproduced with our approach, which can only be seen by looking at the qualitative structure of the resulting surface flow fields. Figure 9b) shows the surface velocity field of simulation 2. The location of tributary 7 and the central stream are well reproduced.

- Especially in the simulations 11-15, with $q = 2$, a much better representation of the central
 25 stream and the inflow into the ice shelf across the grounding line is found, as can be seen

for example in the surface flow field from simulation 11, shown in Fig. 9c. The influence of the effective pressure N_b is thus emphasised. At the same time this method does not lead to a full reproduction of the surface flow structure. This suggests that other processes, not considered here, are also important for the basal sliding behaviour. A possibility, not tested yet due to time constraints (for a detailed description of the solution time of the simulations refer to Wilkens (2014)), is the effect of the basal stress exponent p . Increasing it would possibly to some extent regulate the high velocities in some areas, due to low basal stresses.

4.2.3 Temperature regime

The basal homologous temperature from simulation 2, shown in Fig. 10, shows a very clear structure of the temperate base below the tributaries, even though they are not clearly visible in the flow field (cf. Fig. 9b). The temperature driven separation between tributaries 2 and 4 and tributaries 7 and 9 are even better visible than in the reference simulation (cf. Fig. 7). The structure of the basal homologous temperature of all other simulations look very similar to that of simulation 2, although the total area fraction of ice at pressure melting point varies, as well as the separation between the tributaries.

Another interesting feature found in the structure of the basal temperature from simulation 2 is the advection of warmer ice into the shelf. This feature can be attributed to the implementation of the thermal basal boundary condition in the shelf. While the heat flux is not allowed to raise the temperature above 271.15 K, it does not hinder the advection of warmer ice from the grounded areas.

The structure of the bands of warmer ice agree well with melt channels below the ice shelf as found by Vaughan et al. (2012).

4.3 Parametrisation 2: Li-sliding

4.3.1 Simulation procedure

Another approach to relate the basal roughness to the basal sliding velocity was introduced by Li et al. (2010). We test their idea for applicability to PIG. Li et al. (2010) introduce a two-parameter roughness measure that represents the amplitude ξ_2 and frequency η_2 of the undulations, as described in Sect. 3.1.

For all simulations conducted in this section, only the ice flow model is solved for, due to time constraints (cf. Wilkens (2014)). The temperature distribution within the ice is taken from the reference simulation. The base below the fast flowing areas is thus temperate in all simulations (cf. Fig. 7). Use of the temperature field from the reference simulation gives the opportunity to connect the sliding behaviour to the basal temperature, thus only allowing ice to slide where T is close to T_{pmp} . This was already done in the reference simulation (cf. Sect. 4.1) and the simulations with Parametrisation 1 (cf. Sect. 4.2). The use of the temperature function $f(T)$ slightly reduces the RMS error of the simulated surface velocity field to that of the reference simulation, but does not change the overall picture, as achieved without the use of $f(T)$.

We conduct 18 simulations, whereby the value of C_L (Eq. (18)) is varied in the range $[3 \times 10^{-2}; 3 \times 10^2] \text{ Pa}^{-2} \text{ m a}^{-1}$.

4.3.2 Velocity field

The RMS_{u_s} deviations between the reference and simulated results are shown for all simulations in Fig. 11a, and show a somewhat regular pattern. For the slower flowing areas, the RMS_{u_s} value increases with increasing C_L . For the faster flowing areas, the RMS_{u_s} value first slightly decreases with increasing C_L , and, after reaching a minimum of $\text{RMS}_{u_s} = 500 \text{ m a}^{-1}$ for $C_L = 1.58 \text{ Pa}^{-2} \text{ m a}^{-1}$, increases with increasing C_L . Since we conduct simulations with discrete values for C_L , the value of $\text{RMS}_{u_s} = 500 \text{ m a}^{-1}$ represents the minimum value for the simulations conducted here, and not an absolute minimum. The RMS_{u_s} value

for the entire region "All", shows a similar behaviour of first decreasing and then increasing with increasing C_L , with a minimum RMS_{u_s} value of 271 m a^{-1} for $C_L = 1 \text{ Pa}^{-2} \text{ m a}^{-1}$.

When looking at the structure of the resulting surface flow fields, shown in Fig. 11b and 11c, it is apparent that some features of the observed surface flow field are reproduced.

5 The central stream in all the simulations from this section is partitioned into a faster flowing upper part, and a slower flowing lower part, in the vicinity of the ice shelf.

No single value for C_L could be found, that reproduces the surface velocity field of PIG with all its features. For higher C_L values, that reproduce the velocities in the central stream in a better manner, the velocities in the slower flowing area around tributaries 3, 5, 7 and 9, 10 located to the South of the main stream, are simulated much too high. Additionally, the area around tributary 14 behaves slightly different to most other tributaries. It speeds up much faster for much lower values of C_L . This is related to the low roughness measures ξ_2 and η_2 in that region.

5 Discussion

15 We have shown that the complex surface flow structure of PIG could be well reproduced with our simplified approach of an inversion for a basal sliding parameter β^2 . Although the simulated flow pattern agrees well with observations, some differences in the magnitude of the surface flow velocities were found. These differences are highest in the ice shelf, and might be partly related to a slower inflow from the grounded areas. The simulated velocity is about 1 km a^{-1} slower than the observed surface velocity just before the grounding line in flow direction. This might be due to the position of the grounding line in our model. The grounding line position in our model is further downstream than the location in 2009, to which the observed surface velocity field belongs (2007-2009). Or it might be caused by the method of inferring β^2 , as $\tau_{b, \text{nosl}}$ is not vanishing near the grounding line, as would be expected (compare to Joughin et al. (2010); Morlighem et al. (2010)).

25 The main cause though seems to be that we did not account for the highly rifted shear margins in our model. These shear margins have been shown to be rheologically softer than

undamaged ice (e.g. Humbert et al., 2009). In reality the shear margins partly uncouple the fast flowing central part from the surrounding ice. In our model we treat the shear margins rheologically equal to undamaged ice. This leads to an overestimation of the flow outside the central stream, and an underestimation within the central stream in the main trunk. The softening due to shear margins can be included in different ways, as for example done in Joughin et al. (2010); Favier et al. (2014), and will be included in future model versions.

The use of our high resolution thermo-mechanical full-Stokes model COMice further allowed for an analysis of the thermal structure of the glacier. We found the base of the glacier to be predominantly temperate, especially the fast flowing areas, while the rest of the inner ice body is mainly cold. This finding is consistent with the general definition of an Antarctic glacier, where, due to cold conditions at the surface, the cold-temperate transition surface (CTS) (Blatter and Hutter, 1991) is located at or near the base. To form a significant basal temperate layer Blatter and Hutter (1991) find that strain heating is the necessary or dominant mechanism. This also agrees well with our results, as the flow of PIG is dominated by basal sliding and therefore strain heating due to internal deformation is small. Only an area around tributary 11 (cf. Fig. 7 and 8c), where strain heating is much higher, shows the existence of a somewhat larger temperate layer at the base.

Unfortunately there are no measured temperature profiles available at PIG, to which our results could be compared. Nonetheless our findings of a temperate base below some parts of PIG are supported by findings from Smith et al. (2013), who find hints for the existence of water below the glacier.

As the first new parametrisation for basal sliding we tested the applicability of including actual measured roughness data in a sliding law, to reproduce the surface flow field structure of PIG. As a motivation we use the original ideas that motivated the Weertman-type sliding law, as shown in Eq. (14), and that relate the basal sliding parameter C_b to the basal roughness ξ (Rippin et al., 2011). We combine the spatial distribution of the basal roughness ξ with a plausible range of the basal sliding parameter C_b , to create a new basal sliding parameter C_ξ . This new parameter C_ξ is applied in the basal sliding law in different forms. On the one hand the range of values for C_ξ , on the other hand the influence of the

effective pressure N_b in the sliding law is varied. The variation of the range for C_ξ is done to test the influence of the extreme values onto the flow field. The increase of the influence of the effective pressure N_b is done to investigate the importance of the marine setting, as large parts below the glacier are below sea level.

5 We find that the location of many tributaries can be reproduced with this approach, although not the full complexity of the flow structure. The central stream is in large areas underlain by a very smooth bed, which becomes rougher towards the grounding line. We have shown that, with this approach, for a fast transition across the grounding line, the influence of the effective normal stress N_b onto basal sliding must be large in that area. The
10 low effective normal stress in that area leads to higher basal sliding velocities. This is especially plausible in the vicinity of the grounding line, as part of the overburden pressure is supported by basal water or sea water and basal motion therefore facilitated.

At the same time the method, as applied here, does not lead to a full reproduction of the surface flow structure. This suggests that other processes, not considered here, are also
15 important for the basal sliding behaviour. A possibility not tested yet due to time constraints is the effect of the basal stress exponent p . Increasing it would to some extent perhaps regulate the high velocities in some areas, due to low basal stresses.

The locations of the fast flowing tributaries and the central stream are well indicated by a temperate base. The structure is visible even more clearly than for the reference simulation. This supports the idea that the location of some tributaries is influenced by basal
20 temperatures.

For the second new parametrisation for basal sliding we test the applicability of a theory developed by Li et al. (2010) to the region of PIG, that connects a two-parameter roughness measure $\{\xi_2, \eta_2\}$ to the basal sliding law. We rewrite the equations from Li et al. (2010), by
25 partly using information of the original ideas from Weertman (1957), and extend the sliding law with a temperature function $f(T)$, to apply it as a boundary condition in our flow model. We define a constant sliding parameter C_L , over which a parameter study is conducted.

The results of the surface flow field show certain features. The central stream in all the simulations from this section is partitioned into a faster flowing upper part, and a slower

flowing lower part, in the vicinity of the ice shelf. No single value for C_L could be found, that reproduces the surface velocity field of PIG with all its features. For higher C_L values, that reproduce the velocities in the central stream in a better manner, the velocities in the slower flowing area around tributaries 3, 5, 7 and 9, located to the South of the main stream, are simulated much too high (cf. Fig. 11c). Additionally, the area around tributary 14 behaves slightly different to most other tributaries. It flows much faster for much lower values of C_L . This is related to the low roughness measures ξ_2 and η_2 in that region.

Thus, despite the inability of a complete reproduction of the surface flow field of PIG with the method presented here, it still resulted in a surface flow structure, that reveals some important features, like the location of the fast flowing central stream and some of the numerous tributaries.

6 Conclusions

The overall motion of the fast flowing parts of PIG are dominated by basal motion. The parametrisation of basal motion is therefore crucial for simulating the flow of PIG. Especially when running prognostic simulations of the glacier and aiming at analysing the stability of the system, parametrisation of basal motion is important. High subglacial erosion rates are likely to change the subglacial environment over time. Also the basal temperature plays an important role in separating fast sliding regions from regions dominated by internal deformation. We introduced two different approaches of connecting a basal sliding formulation to an actually measurable subglacial parameter, the basal roughness measure. Our results show, that the roughness measure is a very useful parameter to be considered for parametrisation of basal motion at PIG, as important features of the flow field could be reproduced. Nonetheless the full complexity of the problem was not captured. Our approach is a step towards a more physically based parametrisation for basal sliding, which is very important for realistic simulations of glacier dynamics.

Acknowledgements. This work was supported through the Cluster of Excellence 'CliSAP' (EXC177), University of Hamburg, funded through the German Science Foundation (DFG). We would like to thank Anne Le Brocq for providing the compiled data set for the geometry of Pine Island Glacier.

References

- 5 Bamber, J., Gomez-Dans, J., , and Griggs, J.: A new 1km digital elevation model of the Antarctic derived from combined satellite radar and laser data – Part 1: Data and methods, *THE CRYOSPHERE*, 3, 101–111, doi:10.5194/tc-3-101-2009, 2009.
- Bindschadler, R.: The importance of pressurized subglacial water in separation and sliding at the glacier bed, *J GLACIOL*, 29, 3–19, 1983.
- 10 Bingham, R. and Siegert, M.: Quantifying subglacial bed roughness in Antarctica: implications for ice-sheet dynamics and history, *QUATERNARY SCI REV*, 28, 223–236, 2009.
- Blatter, H. and Hutter, K.: Polythermal conditions in Arctic glaciers, *J GLACIOL*, 37, 261–269, 1991.
- Bohlander, J. and Scambos, T.: Antarctic coastlines and grounding line derived from MODIS Mosaic of Antarctica (MOA), National Snow and Ice Data Center, Digital media, accessed 24 April 2008.,
- 15 Boulder, Colorado USA, 2007.
- Budd, W. and Jenssen, D.: Numerical modelling of the large-scale basal water flux under the West Antarctic Ice Sheet, in: *Dynamics of the West Antarctic Ice Sheet*, edited by Van der Veen, C. J. and Oerlemans, J., p. 293–320, Kluwer, Dordrecht, 1987.
- Codina, R.: Comparison of some finite element methods for solving the diffusion-convection-reaction
- 20 equation, *COMPUT METHOD APPL M*, 156, 185–210, doi:10.1016/S0045-7825(97)00206-5, 1998.
- Comiso, J.: Variability and Trends in Antarctic surface temperatures from in situ and satellite infrared measurements, *J CLIMATE*, 13, 1674–1696, 2000.
- COMSOL: COMSOL Multiphysics Reference Guide, COMSOL AB, Vers. 4.3a, [http://www.comsol.com/\(lastaccess:10August2014\)](http://www.comsol.com/(lastaccess:10August2014)), 2012.
- 25 Cornford, S., Martin, D., Graves, D., Ranken, D., Le Brocq, A., Gladstone, R., Payne, A., Ng, E., and Lipscomb, W.: Adaptive mesh, finite volume modeling of marine ice sheets, *J COMPUT PHYS*, 232, 529–549, 2012.
- Cuffey, K. M. and Paterson, W. S. B.: *The Physics of Glaciers*, Butterworth-Heinemann, 4th edn.,
- 30 2010.

- Dutrieux, P., De Rydt, J., Jenkins, A., Holland, P., Ha, H., Lee, S., Steig, E., Ding, Q., Abrahamsen, E., and Schröder, M.: Strong sensitivity of Pine Island ice-shelf melting to climatic variability, *SCIENCE*, 343, 174–178, 2014.
- Favier, L., Durand, G., Cornford, S., Gudmundsson, G., Gagliardini, O., Gillet-Chaulet, F., Zwinger, T., Payne, A., and Le Brocq, A.: Retreat of Pine Island Glacier controlled by marine ice-sheet instability, *NATURE CLIMATE CHANGE*, 4, 117–121, doi:10.1038/NCLIMATE2094, 2014.
- Fowler, A.: A sliding law for glaciers of constant viscosity in the presence of subglacial cavitation, *P R SOC A*, 407, 147–170, 1986.
- Fox Maule, C., Purucker, M., Olsen, N., and Mosegaard, K.: Heat flux anomalies in Antarctica revealed by satellite magnetic data, *SCIENCE*, 309, 464–467, 2005.
- Gladstone, R., Lee, V., Rougier, J., Payne, A., Hellmer, H., Brocq, A. L., Shepherd, A., Edwards, T., Gregory, J., and Cornford, S.: Calibrated prediction of Pine Island Glacier retreat during the 21st and 22nd centuries with a coupled flowline model, *EARTH PLANET SC LETT*, 333-334, 191–199, 2012.
- Glen, J.: The creep of polycrystalline ice, *P R SOC A*, 228, 519–538, 1955.
- Greve, R. and Blatter, H.: *Dynamics of Ice Sheets and Glaciers*, Springer, Berlin, Heidelberg, 2009.
- Gudmundsson, G., Krug, J., Durand, G., Favier, L., and Gagliardini, O.: The stability of grounding lines on retrograde slopes, *THE CRYOSPHERE*, 6, 1497–1505, doi:10.5194/tc-6-1497-2012, 2012.
- Hauke, G. and Hughes, T. J.: A comparative study of different sets of variables for solving compressible and incompressible flows, *COMPUT METHOD APPL M*, 153, 1–44, doi:10.1016/S0045-7825(97)00043-1, 1998.
- Hooke, R. L.: *Principles of Glacier Mechanics*, Cambridge University Press, Cambridge, 2005.
- Horwath, M. and Dietrich, R.: Signal and error in mass change inferences from GRACE: the case of Antarctica, *GEOPHYS J INT*, 177, 849–864, 2009.
- Hubbard, B., Siegert, M., and McCarroll, D.: Spectral roughness of glaciated bedrock geomorphic surfaces: implications for glacier sliding, *J GEOPHYS RES*, 105, 21 295–21 303, 2000.
- Hughes, T.: Is the West Antarctic ice sheet disintegrating?, *J GEOPHYS RES*, 78, 7884–7910, 1973.
- Humbert, A., Kleiner, T., Mohrholz, C., Oelke, C., Greve, R., and Lange, M.: A comparative modeling study of the Brunt Ice Shelf/Stancomb-Wills Ice Tongue system, East Antarctica, *J GLACIOL*, 55, 53–65, 2009.
- Hutter, K.: *Theoretical glaciology: Material Science of Ice and the Mechanics of Glaciers and Ice Sheets*, Reidel, Tokyo, 1983.

- Huybrechts, P.: The Antarctic ice sheet and environmental change: a three-dimensional modelling study, *REPORTS ON POLAR RESEARCH*, Alfred Wegener Institute for Polar and Marine Research, Bremerhaven, 99, 1992.
- 5 Joughin, I., Tulaczyk, S., Bamber, J., Blankenship, D., Holt, J., Scambos, T., and Vaughan, D.: Basal conditions for Pine Island and Thwaites Glaciers, West Antarctica, determined using satellite and airborne data, *J GLACIOL*, 55, 245–257, 2009.
- Joughin, I., Smith, B., and Holland, D.: Sensitivity of 21st century sea level to ocean-induced thinning of Pine Island Glacier, Antarctica, *GEOPHYS RES LETT*, 37, L20502, doi:10.1029/2010GL044819, 2010.
- 10 Kamb, B.: Sliding motion of glaciers: theory and observations, *Reviews of Geophysics and Space Physics*, 8, 673–728, 1970.
- Karlsson, N., Rippin, D., Vaughan, D., and Corr, H.: The internal layering of Pine Island Glacier, West Antarctica, from airborne radar-sounding data, *ANN GLACIOL*, 50, 141–146, 2009.
- Katz, R. and Worster, M.: Stability of ice-sheet grounding lines, *P R SOC A*, 466, 1597–1620, 2010.
- 15 Kleiner, T. and Humbert, A.: Numerical simulations of major ice streams in western Dronning Maud Land, Antarctica, under wet and dry basal conditions, *J GLACIOL*, 60, 215–232, 2014.
- Le Brocq, A., Payne, A., and Vieli, A.: An improved Antarctic dataset for high resolution numerical ice sheet models (ALBMAP v1), *EARTH SYST SCI DATA*, 2, 247–260, doi:10.5194/essd-2-247-2010, 2010.
- 20 Leguy, G. R., Asay-Davis, X. S., and Lipscomb, W. H.: Parameterization of basal friction near grounding lines in a one-dimensional ice sheet model, *THE CRYOSPHERE*, 8, 1239–1259, doi:10.5194/tc-8-1239-2014, 2014.
- Li, X., Sun, B., Siegert, M., Bingham, R., Tang, X., Zhang, D., Cui, X., and Zhang, X.: Characterization of subglacial landscapes by a two-parameter roughness index, *J GLACIOL*, 56, 831–836, 2010.
- 25 MacAyeal, D.: The basal stress distribution of Ice Stream E, Antarctica, inferred by control methods, *J GEOPHYS RES*, 97, 595–603, 1992.
- Morland, L.: Thermomechanical balances of ice sheet flows, *GEOPHYS ASTRO FLUID*, 29, 237–266, 1984.
- 30 Morlighem, M., Rignot, E., Seroussi, H., Larour, E., Ben Dhia, H., and Aubry, D.: Spatial patterns of basal drag inferred using control methods from a full-Stokes and simpler models for Pine Island Glacier, West Antarctica, *GEOPHYS RES LETT*, 37, L14 502, doi:10.1029/2010GL043853, 2010.

- Mouginot, J., Rignot, E., and Scheuchl, B.: Sustained increase in ice discharge from the Amundsen Sea Embayment, West Antarctica, from 1973 to 2013, *GEOPHYS RES LETT*, 41, 1576–1584, doi:10.1002/2013GL059069, 2014.
- 5 Nye, J.: The distribution of stress and velocity in glaciers and ice-sheets, *P R SOC A*, 239, 113–133, 1957.
- Nye, J.: The calculation of sliding of ice over a wavy surface using Newtonian viscous approximation, *P R SOC A*, A311, 445–467, 1969.
- Park, J., Gourmelen, N., Shepherd, A., Kim, S., Vaughan, D., and Wingham, D.: Sustained retreat of the Pine Island Glacier, *GEOPHYS RES LETT*, 40, 1–6, 2013.
- 10 Paterson, W.: *The Physics of Glaciers*, Elsevier, Oxford, 1994.
- Pattyn, F.: A new three-dimensional higher-order thermomechanical ice sheet model: basic sensitivity, ice stream development, and ice flow across subglacial lakes, *J GEOPHYS RES*, 108, 2382, doi:10.1029/2002JB002329, 2003.
- Pattyn, F., Perichon, L., Durand, G., Favier, L., Gagliardini, O., Hindmarsh, R. C., Zwinger, T., Albrecht, T., Cornford, S., Docquier, D., Fürst, J., Goldberg, D., Gudmundsson, H., Humbert, A., Hutten, M., Huybrechts, P., Jouvét, G., Kleiner, T., Larour, E., Martin, D., Morlighem, M., Payne, A., Pollard, D., Rückamp, M., Rybak, O., Seroussi, H., Thoma, M., and Wilkens, N.: Grounding-line migration in plan-view marine ice-sheet models: results of the ice2sea MISMIP3d intercomparison, *J GLACIOL*, 59, 2163, doi:10.3189/2013JoG12J129, 2013.
- 15 Rignot, E.: Fast recession of a West Antarctic glacier, *SCIENCE*, 281, 549–551, 1998.
- Rignot, E.: Ice-shelf changes in Pine Island Bay, Antarctica, 1947-2000, *J GLACIOL*, 48, 247–256, 2002.
- Rignot, E.: Changes in West Antarctic ice stream dynamics observed with ALOS PALSAR data, *GEOPHYS RES LETT*, 35, L12505, doi:10.1029/2008GL033365, 2008.
- 20 Rignot, E., Mouginot, J., and Scheuchl, B.: Ice flow of the Antarctic ice sheet, *SCIENCE*, 333, 1427–1430, 2011.
- Rippin, D., Vaughan, D., and Corr, H.: The basal roughness of Pine Island Glacier, West Antarctica, *J GLACIOL*, 57, 67–76, 2011.
- Rippin, D., Bingham, R., Jordan, T., Wright, A., Ross, N., Corr, H., Ferraccioli, F., Le Brocq, A., Rose, K., and Siegert, M.: Basal roughness of the Institute and Möller Ice Streams, West Antarctica: process determination and landscape interpretation, *GEOMORPHOLOGY*, 214, 139–147, 2014.
- 25 Rückamp, M.: *Eisgeometrie und Fließdynamik der subpolaren Eiskappe von King George Island (Antarktis)*, Ph.D. thesis, Universität Münster, Münster, 2011.

- Schmeltz, M., Rignot, E., Dupont, T., and MacAyeal, D.: Sensitivity of Pine Island Glacier, West Antarctica, to changes in ice-shelf and basal conditions: a model study, *J GLACIOL*, 48, 552–558, 2002.
- 5 Seroussi, H., Morlighem, M., Rignot, E., Mouginot, J., Larour, E., Schodlok, M., and Khazendar, A.: Sensitivity of the dynamics of Pine Island Glacier, West Antarctica, to climate forcing for the next 50 years, *THE CRYOSPHERE DISCUSS*, 8, 1873–1894, doi:10.5194/tcd-8-1873-2014, 2014.
- Shepherd, A., Ivins, E. R., A. G., Barletta, V. R., Bentley, M. J., Bettadpur, S., Briggs, K. H., Bromwich, D. H., Forsberg, R., Galin, N., Horwath, M., Jacobs, S., Joughin, I., King, M. A., Lenaerts, J. T. M., Li, J., Ligtenberg, S. R. M., Luckman, A., Luthcke, S. B., McMillan, M., Meister, R., Milne, G.,
10 Mouginot, J., Muir, A., Nicolas, J. P., Paden, J., Payne, A. J., Pritchard, H., Rignot, E., Rott, H., Sandberg Sørensen, L., Scambos, T. A., Scheuchl, B., Schrama, E. J. O., Smith, B., Sundal, A. V., van Angelen, J. H., van de Berg, W. J., van den Broeke, M. R., Vaughan, D. G., Velicogna, I., Wahr, J., Whitehouse, P. L., Wingham, D. J., Yi, D., Young, D., and Zwally, H. J.: A reconciled estimate of ice-sheet mass balance, *SCIENCE*, 338, 1183–1189, 2012.
- 15 Smith, A., Bentley, C., Bingham, R., and Jordan, T.: Rapid subglacial erosion beneath Pine Island Glacier, West Antarctica, *GEOPHYS RES LETT*, 39, L12501, doi:10.1029/2012GL051651, 2012.
- Smith, A., Jordan, T., Ferraccioli, F., and Bingham, R.: Influence of subglacial conditions on ice stream dynamics: Seismic and potential field data from Pine Island Glacier, West Antarctica, *J GEOPHYS RES*, 118, 1471–1482, 2013.
- 20 Stenoien, M. and Bentley, C.: Pine Island Glacier, Antarctica: A study of the catchment using interferometric synthetic aperture radar measurements and radar altimetry, *J GEOPHYS RES*, 105, 21 761–21 779, 2000.
- Taylor, J., Siegert, M. J., Payne, A. J., and Hubbard, B.: Regional-scale bed roughness beneath ice masses: measurement and analysis, *COMPUT GEOSCI*, 30, 899–908, 2004.
- 25 Vaughan, D.: West Antarctic Ice Sheet collapse - the fall and rise of a paradigm, *CLIMATIC CHANGE*, 91, 65–79, 2008.
- Vaughan, D., Corr, H., Ferraccioli, F., Frearson, N., O'Hare, A., Mach, D., Holt, J., Blankenship, D., Morse, D., and Young, D.: New boundary conditions for the West Antarctic ice sheet: subglacial topography beneath Pine Island Glacier, *GEOPHYS RES LETT*, 33, L09501, doi:10.1029/2005GL025588, 2006.
- 30 Vaughan, D., Corr, H., Bindschadler, R., Dutrieux, P., Gudmundsson, G., Jenkins, A., Newman, T., Vornberger, P., and Wingham, D.: Subglacial melt channels and fracture in the floating part of Pine Island Glacier, Antarctica, *J GEOPHYS RES*, 117, F03012, doi:10.1029/2012JF002360, 2012.

Weertman, J.: On the sliding of glaciers, *J GLACIOL*, 3, 33–38, 1957.

Weis, M., Greve, R., and Hutter, K.: Theory of shallow ice shelves, *CONTINUUM MECH THERM*, 11, 15–50, 1999.

5 Wilkens, N.: Pine Island Glacier - a 3D full-Stokes model study, Ph.D. thesis, Universität Hamburg, Hamburg, <http://ediss.sub.uni-hamburg.de/volltexte/2014/6735/>, [http://ediss.sub.uni-hamburg.de/volltexte/2014/6735/\(lastaccess:18August2014\)](http://ediss.sub.uni-hamburg.de/volltexte/2014/6735/(lastaccess:18August2014)), 2014.

Wingham, D., Wallis, D., and Shepherd, A.: Spatial and temporal evolution of Pine Island Glacier thinning, 1995–2006, *GEOPHYS RES LETT*, 36, L17 501, doi:10.1029/2009GL039126, 2009.

Table 1. Parameter Values

Parameter	Value	Unit	Description
ρ_i	918	kg m^{-3}	Ice density
ρ_{sw}	1028	kg m^{-3}	Seawater density
g	9.81	m s^{-2}	Acceleration of gravity
n	3		Stress exponent
R	8.314	$\text{J mol}^{-1} \text{K}^{-1}$	Gas constant
Q	60 for $T' \leq 263.15 \text{ K}$ 139 for $T' > 263.15 \text{ K}$	kJ mol^{-1}	Activation energy for creep (Paterson, 1994)
A_0	3.985×10^{-13} for $T' \leq 263.15 \text{ K}$ 1.916×10^3 for $T' > 263.15 \text{ K}$	$\text{s}^{-1} \text{Pa}^{-3}$	Pre-exponential constant (Paterson, 1994)
T_0	273.15	K	Melting point for low pressures
β_c	9.8×10^{-8}	K Pa^{-1}	Clausius-Clapeyron constant (Hooke, 2005)
T_{sw}	271.15	K	Freezing temperature of seawater
ν	0.1		Submelt sliding parameter (Budd and Jenssen, 1987)
$\kappa(T)$	$9.828 e^{(-5.7 \times 10^{-3} T [\text{K}^{-1}])}$	$\text{W m}^{-1} \text{K}^{-1}$	Thermal conductivity
$c_p(T)$	$152.5 + 7.122 T [\text{K}^{-1}]$	$\text{J kg}^{-1} \text{K}^{-1}$	Specific heat capacity
z_{sl}	0	m	Sea level
spy	31536000	s a^{-1}	Seconds per year

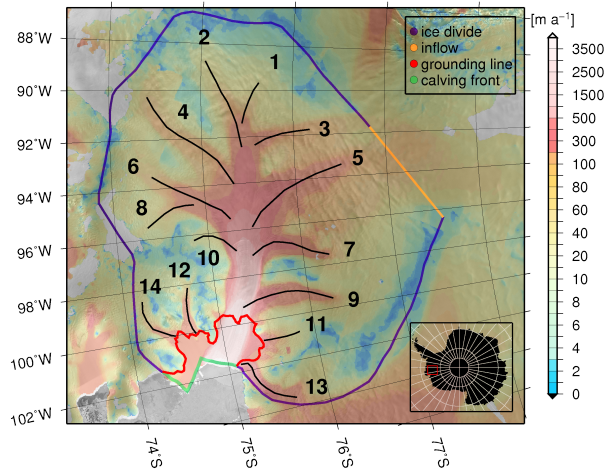


Figure 1. RADARSAT Antarctic Mapping Project (RAMP) Mosaic with the observed surface velocities from Rignot et al. (2011) and the model domain of Pine Island Glacier, with the different lateral boundaries, the grounding line and the numbered tributaries indicated.

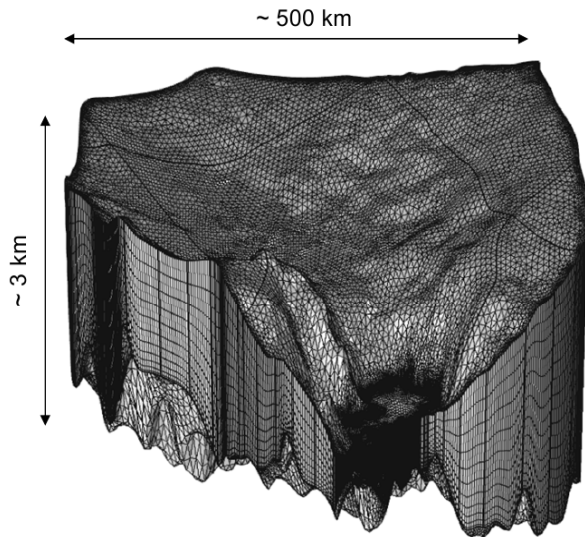


Figure 2. FEM mesh on the 3D Pine Island Glacier model geometry.

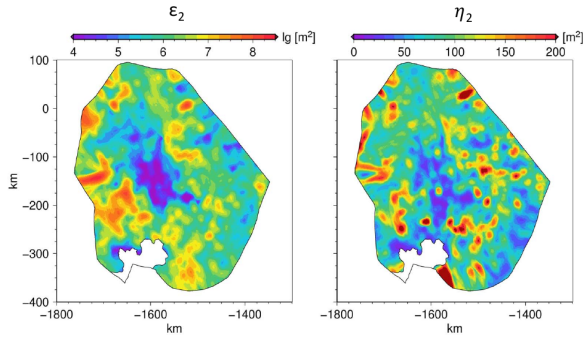


Figure 3. The two-parameter roughness measure at Pine Island Glacier, given by the roughness amplitude ξ_2 and the roughness frequency η_2 .

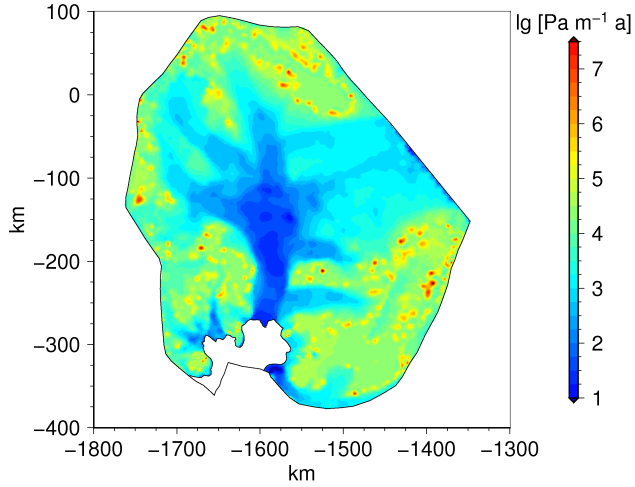


Figure 4. Spatial distribution of the basal sliding parameter β^2 .

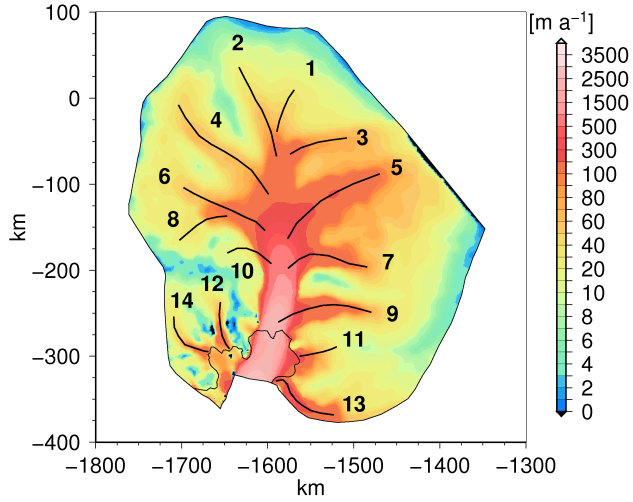


Figure 5. Surface velocity field from the reference simulation $|u_{s,\text{ref}}|$, with the numbered tributaries.

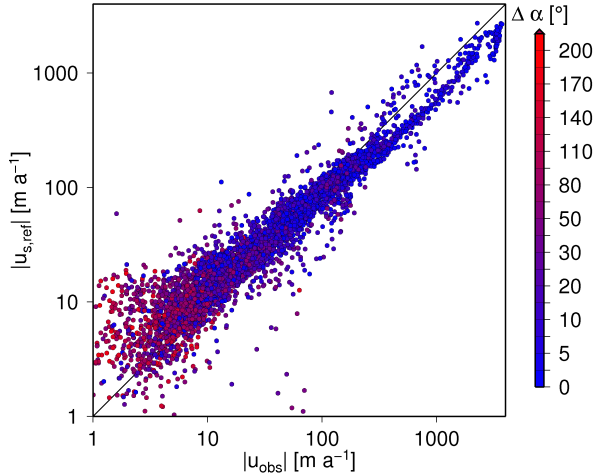


Figure 6. Observed surface velocity field $|u_{\text{obs}}|$ vs. reference surface velocity field $|u_{\text{s,ref}}|$. The logarithmic scales exaggerate the spread around the low speeds. The angle offset $\Delta\alpha$ between the vectors of the surface velocity field u_{obs} and the reference surface velocity field $u_{\text{s,ref}}$ is shown as the colour code.

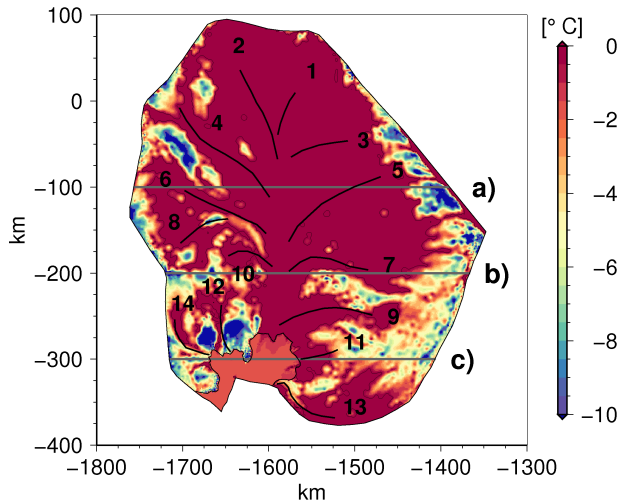


Figure 7. The basal homologous temperature from the reference simulation $T'_{D,ref}$, with tributary locations in black and the location of the vertical slices a), b) and c) in Fig. 8 in grey.

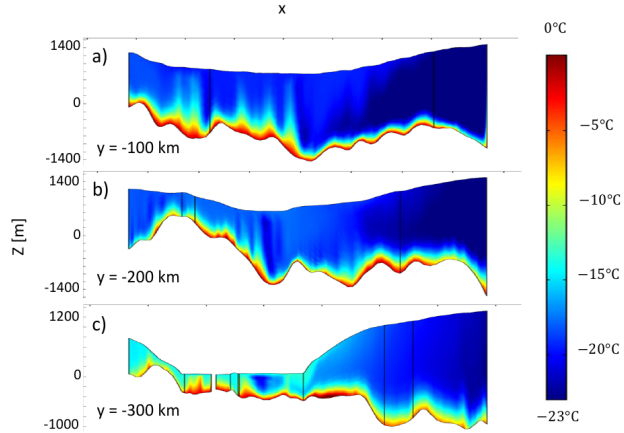


Figure 8. The internal homologous temperature from the reference simulation T'_{ref} at three vertical slices a), b) and c) (horizontal locations indicated in Fig. 7)

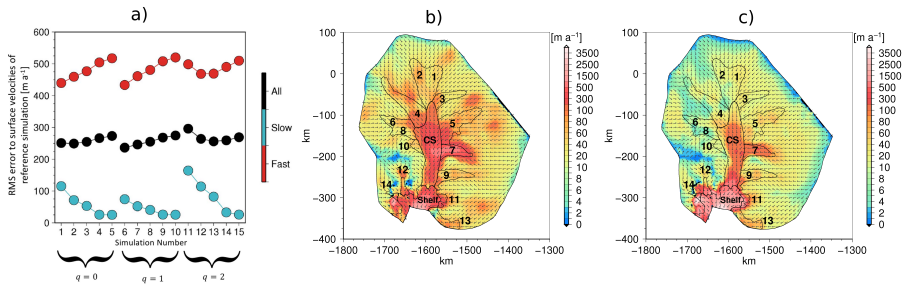


Figure 9. a) RMS error to the surface velocity field of the reference simulation versus the simulation number; b) Surface velocity field of simulation 2 with $q = 0$; c) Surface velocity field of simulation 11 with $q = 2$.

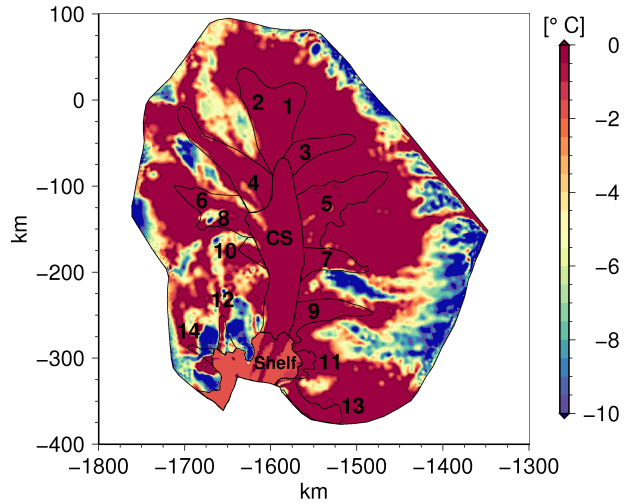


Figure 10. Basal homologous temperature of simulation 2 $T'_{b,p1q0_2}$.

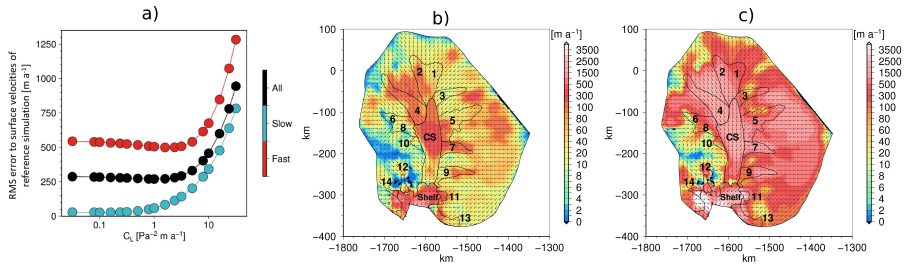


Figure 11. a) RMS error to the surface velocity field of the reference simulation versus C_L value; b) Surface velocity field with $C_L = 1 \text{ Pa}^{-2} \text{m a}^{-1}$; c) Surface velocity field with $C_L = 31.56 \text{ Pa}^{-2} \text{m a}^{-1}$.